Translating imaging traits of mass-forming intrahepatic cholangiocarcinoma into the clinic: From prognostic to therapeutic insights

Authors

Gu-Wei Ji, Qing Xu, Chen-Yu Jiao, Ming Lu, Zheng-Gang Xu, Biao Zhang, Yue Yang, Ke Wang, Xiang-Cheng Li, Xue-Hao Wang

Correspondence

wangxh@njmu.edu.cn (X.-H. Wang), drxcli@njmu.edu.cn (X.-C. Li), 13776683209@163.com (Q. Xu).

Graphical abstract

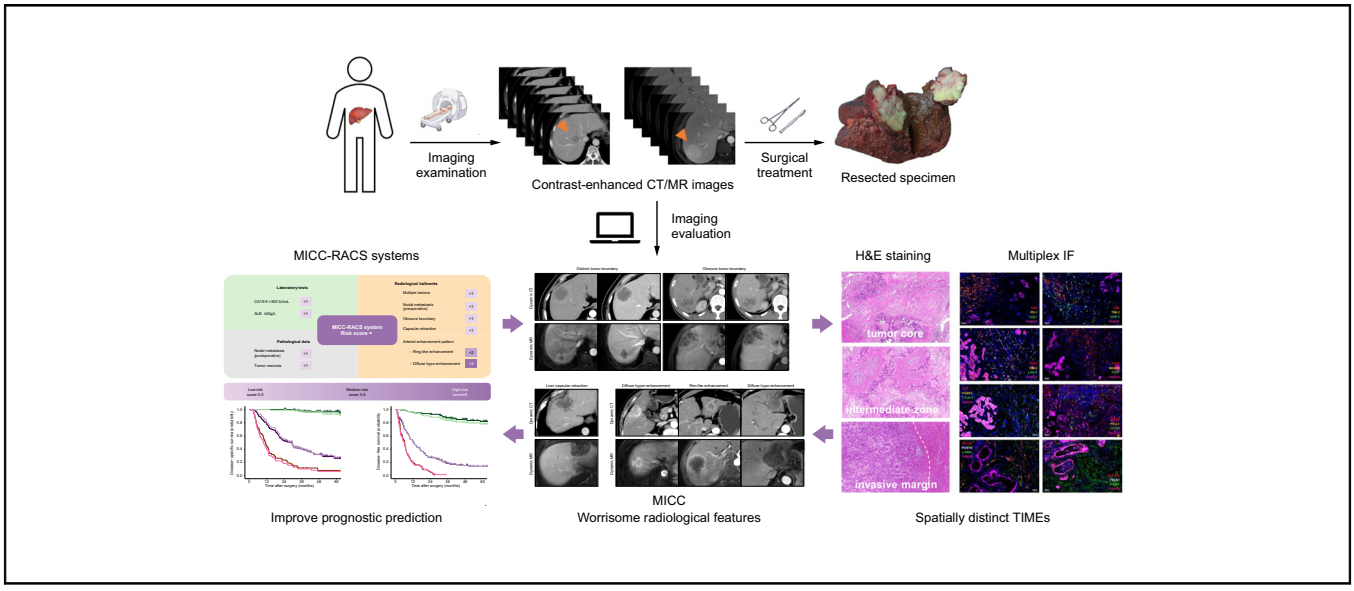

Highlights

- We proposed novel and simple but powerful prognostic tools for MICC.
- MICC-RACS systems can predict the prognosis either before or after surgery.
- MICC-RACS systems outperform rival models and staging systems.
- Radiological traits integrated into systems are highly correlated with TIMEs.
- MICC-RACS systems may facilitate patient-tailored immunotherapy approach.

Impact and Implications

The progress toward clinical translation of imaging biomarkers for mass-forming intrahepatic cholangiocarcinoma (MICC) is slower than anticipated. Questions remain on the biologic behaviour of MICC underlying imaging traits. In this study, we proposed novel and easy-to-use tools, built on radiological and clinical features, that demonstrated good performance in predicting the prognosis either before or after surgery and outperformed rival models/systems across major imaging modalities. The characteristic radiological traits integrated into prognostic systems (arterial enhancement pattern, tumour boundary, and capsular retraction) were highly correlated with heterogeneous tumour-immune microenvironments, thereby renovating treatment paradigms for this difficult-to-treat disease.

https://doi.org/10.1016/j.jhepr.2023.100839

Research article

JHEP|Reports

Translating imaging traits of mass-forming intrahepatic cholangiocarcinoma into the clinic: From prognostic to therapeutic insights

Gu-Wei Ji,[1,2,3] Qing Xu,[4,*] Chen-Yu Jiao,[1,2,3] Ming Lu,[4] Zheng-Gang Xu,[1,2,3] Biao Zhang,[5] Yue Yang,[6] Ke Wang,[1,2,3] Xiang-Cheng Li,[1,2,3,*] Xue-Hao Wang[1,2,3,*]

[1]Hepatobiliary Center, The First Affiliated Hospital of Nanjing Medical University, Nanjing, PR China; [2]Key Laboratory of Liver Transplantation, Chinese Academy of Medical Sciences, Nanjing, PR China; [3]NHC Key Laboratory of Living Donor Liver Transplantation (Nanjing Medical University), Nanjing, PR China; [4]Department of Radiology, The First Affiliated Hospital of Nanjing Medical University, Nanjing, PR China; [5]Department of General Surgery, Yancheng No.1 People's Hospital, Yancheng, PR China; [6]Department of General Surgery, The First People's Hospital of Changzhou, Changzhou, PR China

JHEP Reports **2023.** https://doi.org/10.1016/j.jhepr.2023.100839

Background & Aims: The progress toward clinical translation of imaging biomarkers for mass-forming intrahepatic cholangiocarcinoma (MICC) is slower than anticipated. Questions remain on the biologic behaviour underlying imaging traits. We developed and validated imaging-based prognostic systems for resected MICCs with an appraisal of the tumour immune microenvironment (TIME) underpinning patient-specific imaging traits.
Methods: Between January 2009 and December 2019, a total of 322 patients who underwent dynamic computed tomography/magnetic resonance imaging and curative-intent resection for MICC at three hepatobiliary institutions were retrospectively recruited, divided into training (n = 193) and validation (n = 129) datasets. Two radiological and clinical scoring (RACS) systems, one integrating preoperative variables and one integrating preoperative and postoperative variables, were developed using Cox regression analysis. We then prospectively analysed the TIME of tissue samples from 20 patients who met study criteria from January 2021 to December 2021 using multiplexed immunofluorescence.
Results: Preoperative and postoperative MICC-RACS systems built on carbohydrate antigen 19-9, albumin, tumour number, radiological/pathological nodal status, pathological necrosis, and three radiological traits (arterial enhancement pattern, tumour boundary, and capsular retraction) demonstrated good performance in predicting disease-specific (C-statistic >0.80) and disease-free (C-statistic >0.75) survival that outperformed rival models and staging systems across study cohorts (P <0.05 for all). Patients with MICC-RACS score of 0–2 (low risk), 3–5 (medium risk), and ≥6 (high risk) had incrementally worse prognosis after surgery. Significant differences in spatial distribution and infiltration level of immune cells were identified between arterial enhancement patterns. Enhanced infiltration of immunosuppressive regulatory T cells and M2-like macrophages at the invasive margin were noted in tumours with distinct boundary and capsular retraction, respectively.
Conclusions: Our MICC-RACS systems are simple but powerful prognostic tools that may facilitate the understanding of spatially distinct TIMEs and patient-tailored immunotherapy approach.
Impact and Implications: The progress toward clinical translation of imaging biomarkers for mass-forming intrahepatic cholangiocarcinoma (MICC) is slower than anticipated. Questions remain on the biologic behaviour of MICC underlying imaging traits. In this study, we proposed novel and easy-to-use tools, built on radiological and clinical features, that demonstrated good performance in predicting the prognosis either before or after surgery and outperformed rival models/systems across major imaging modalities. The characteristic radiological traits integrated into prognostic systems (arterial enhancement pattern, tumour boundary, and capsular retraction) were highly correlated with heterogeneous tumour-immune microenvironments, thereby renovating treatment paradigms for this difficult-to-treat disease.

Keywords: Intrahepatic cholangiocarcinoma; Radiological traits; Cancer prognosis; Prediction model; Tumour immune microenvironment.
Received 31 January 2023; received in revised form 23 March 2023; accepted 16 June 2023; available online 4 July 2023
* Corresponding authors. Address: Hepatobiliary Center, The First Affiliated Hospital of Nanjing Medical University, 300 Guangzhou Road, Nanjing, 210029, PR China. Tel: +86-13305178713; Fax: +86-68136450 (X.H. Wang); Hepatobiliary Center, The First Affiliated Hospital of Nanjing Medical University, 300 Guangzhou Road, Nanjing, 210029, PR China. Tel.: +86-18951999088; Fax: +86-68136450 (X.C. Li); Department of Radiology, The First Affiliated Hospital of Nanjing Medical University, 300 Guangzhou Road, Nanjing, 210029, PR China. Tel.: +86-13776683209; Fax: +86-68136450 (Q. Xu).
E-mail addresses: wangxh@njmu.edu.cn (X.-H. Wang), drxcli@njmu.edu.cn (X.-C. Li), 13776683209@163.com (Q. Xu).

Introduction

Intrahepatic cholangiocarcinoma (ICC) represents the second most common primary liver malignancy after hepatocellular carcinoma, accounting for 10–15% of all primary liver tumours, and its incidence has been rising in the past few decades worldwide.[1–3] Mass-forming ICC (MICC) is the most common morphological subtype (more than 85% of cases), and therefore, ICC is usually detected as a liver mass lesion.[3] Unfortunately, MICC is a highly lethal liver neoplasm with poor prognosis, high mortality rates, and limited treatment options. Liver resection remains the only potentially curative treatment modality for MICC, but recurrence rates are high and 5-year survival following resection ranges from 25 to 40%.[4,5]

Substantial heterogeneity exists in resected MICC regarding patients' prognosis, and therefore, accurate estimates of outcomes, either preoperatively or postoperatively, are critical to make informed therapeutic decisions. The most commonly used staging schema is the tumour–node–metastasis (TNM) system developed by the American Joint Committee on Cancer; however, the TNM system has been criticised for its limited predictive power.[1] Strategies to incorporate standard patient demographic and clinicopathological traits into models have been adopted to better personalise prognostic estimates; however, the computational complexity and suboptimal ability of these models limit their utility in patient care, even if they are validated.[6–9]

Given the indispensable role of imaging in MICC management, investigators have attempted to explore non-invasive imaging biomarkers for accurate differential diagnosis as well as prediction of pathological grade and subtype.[10–12] Studies have also documented the potential prognostic value of radiological traits at dynamic computed tomography (CT)/magnetic resonance (MR) imaging for patients with MICC.[13–15] However, the progress toward clinical translation has been slower than anticipated despite extensive investigations. Some modality-specific traits, such as degree of diffusion restriction, suffer from limited reproducibility and generalisability considering that one imaging modality, either multiphasic CT or contrast-enhanced MR imaging, is preferred for MICC staging and resectability assessment in clinical practice. Therefore, a cross-modality study strategy may lead to the discovery and validation of unifying imaging traits that are readily comparable across different imaging modalities, which will advance future translational research. In addition, questions remain on how we can better decode the biologic behaviour underlying prognostic imaging traits for MICC.

In this study, we sought to propose simple and readily applicable scoring systems that integrated radiological traits with clinicopathological factors to predict prognosis for surgically treated patients with MICC. The prognostic and predictive efficacy of our scoring systems was compared with that of rival models and staging systems. We further provided a critical appraisal of the tumour immune microenvironment (TIME) underpinning the macroscopic radiological traits that can facilitate therapeutic selection.

Patients and methods

The institutional review boards of all collaborating institutions approved the study protocol (No. 2020-SR-566) and waived the requirement to obtain written informed consent.

Study design and patients

From January 2009 to December 2019, a total of 368 consecutive patients who were evaluated with dynamic CT or MRI and underwent curative-intent liver resection for pathology-proven MICC at three hepatobiliary institutions (The First Affiliated Hospital of Nanjing Medical University, Yancheng No.1 People's Hospital, and The First People's Hospital of Changzhou) were retrospectively reviewed. Patients were excluded for (1) macroscopically positive surgical margins, (2) distant metastatic diseases, (3) CT or MR examinations over 1 month before surgery, (4) prior interventions (such as repeat liver resection, local ablation, transhepatic artery embolisation, chemotherapy, or radiotherapy), (5) other primary malignancies before MICC diagnosis, and (6) lack of follow-up data. A total of 322 patients (median age, 61 years; IQR, 50–68 years; 183 men) were recruited in the final analytic cohort (contrast-enhanced CT, n = 243; extracellular contrast-enhanced MR, n = 11; gadoxetic acid-enhanced MR, n = 68). Eligible patients were randomly separated in a 3:2 ratio into training (n = 193) and validation (n = 129) datasets. A follow-up protocol is described in Supplementary methods.

From January 2021 to December 2021, we prospectively collected specimens from 20 consecutive patients (median age, 64 years; IQR, 57–71 years; 13 men) diagnosed with MICC who underwent preoperative dynamic CT (n = 17) or gadoxetic acid-enhanced MR (n = 3) examination and curative-intent resection at The First Affiliated Hospital of Nanjing Medical University according to the above-mentioned criteria. Tissue samples from three distinct regions of each primary tumour, designated as tumour core, intermediate zone, and invasive margin, were obtained and analysed. A study flowchart is shown in Fig. 1.

Radiological analysis

Technical specifications of contrast-enhanced CT and MR imaging are described in Supplementary methods. Radiological analysis was independently performed by two abdominal radiologists (reader 1 [ML] and reader 2 [QX] with 3 and 20 years of experience in liver imaging, respectively) and two hepatobiliary surgeons (reader 3 [GWJ] and reader 4 [CYJ] with 8 and 10 years of experience in hepatobiliary surgery and imaging, respectively) who were aware of the diagnosis of MICC but blinded to other clinicopathological information. All readers followed a lecture-based training session wherein standardised lexicons with representative images were outlined to allow for targeted evaluation of individual observations. The following imaging traits classified into two major categories were recorded for each patient: (1) conventional traits (tumour number [solitary or multiple], maximum tumour diameter, tumour location [peripheral or perihilar], liver cirrhosis [present or absent], vascular invasion [present or absent], nodal metastasis [present or absent], and peritumoural biliary dilatation [present or absent]) and (2) characteristic traits (gross type [parenchymal-type or ductal-type],[16] tumour boundary [distinct or obscure], arterial enhancement pattern [diffuse hyperenhancement, peripheral rim enhancement, or diffuse hypoenhancement], progressive enhancement [present or absent], enhancing capsule [present or absent], capsular retraction [present or absent], and peripheral washout [present or absent]).

Diffuse hyperenhancement was defined as the hyperenhanced area that was >70% of the tumour volume at the

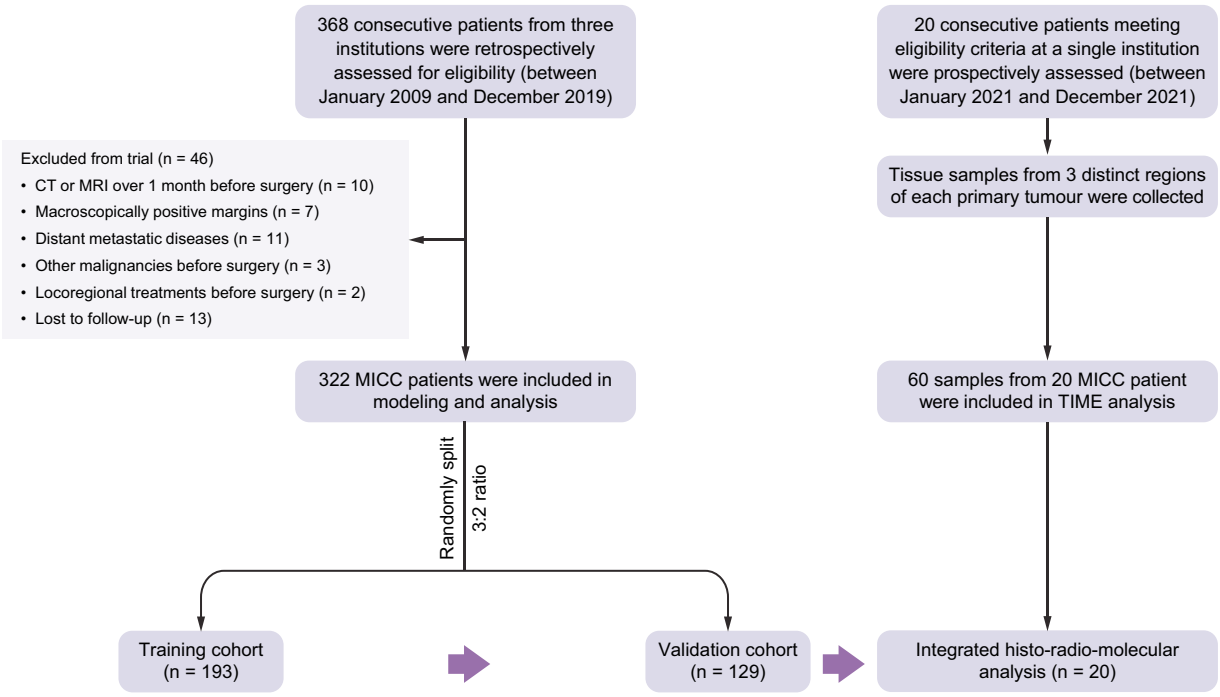

Fig. 1. Study flow diagram. CT, computed tomography; MICC, mass-forming intrahepatic cholangiocarcinoma; MRI, magnetic resonance imaging; TIME, tumour immune microenvironment.

arterial phase; peripheral rim enhancement was defined as the ring-like hyperenhanced area that measured 10–70% of the tumour volume with relatively hypoenhanced central areas.[14] Distinct tumour boundary was defined as a regular and smooth border at either the arterial or venous phase; obscure tumour boundary was defined as an irregular and ill-defined border.[17] Nodal metastasis was defined as a short-axis diameter of larger than 10 mm or central necrosis, as previously described.[15,18] When a patient had multiple tumours, traits of the largest tumour were recorded. The interobserver variability was assessed by means of *k* statistics after independent image review. Any discrepancies in radiological interpretations were resolved by a joint review to reach a consensus. Definitions and examples for major traits are summarised in Fig. 2 and Fig. S1.

TIME evaluation

We evaluated tumour-infiltrating immune cells and cancer-associated fibroblasts (CAFs) in the context of intertumour and intratumour heterogeneity using multiplex immunofluorescence staining under pathologist supervision (JSW and WBH, blinded to the patients' information). Quantification of immune cells (T lymphocytes, natural killer [NK] cells, and macrophages) with co-inhibitory receptors (programmed cell death protein 1 [PD-1]/programmed death-ligand 1 [PD-L1], T-cell Ig and mucin domain-3 protein [TIM-3], lymphocyte-activation gene 3 [LAG-3], cytotoxic T lymphocyte antigen-4 [CTLA-4], T-cell Ig and immunoreceptor tyrosine-based inhibitory motif domain (TIGIT), and NK group 2 member A [NKG2A]) was performed using Quant Center 2.1 (3DHISTECH, Budapest, Hungary) and validated by manual counting of five independent fields with the densest stained cells at 400 × magnification. Immune cell density (number/mm^2) was defined as the mean number of all fields from each sample. Meanwhile, single-cell RNA-sequencing analyses from human ICC samples have highlighted distinct CAF subclusters.[19] CAF subpopulations were identified by representative markers: α-SMA for canonical fibroblast marker, and CD146, POSTN, FBLN1, and HLA-DR for vascular, matrix, inflammatory, and antigen-presenting CAFs, respectively. Fluorescence intensity of the targeted marker was quantified using ImageJ software, and the mean pixel intensity of five densest-stained fields in the stromal compartment was used for statistical analysis. Detailed information of experimental design, antibodies, and staining protocols is described in Fig. 3 and Supplementary methods.

Statistical analysis

Patient characteristics were reported as either median (IQR) or number (percentages), and compared using the Mann–Whitney *U* test, Kruskal–Wallis test, or χ^2 test, unless specified. Two endpoints were analysed: disease-free survival (DFS), defined as the time from surgery to the first recorded disease recurrence, and disease-specific survival (DSS), defined as the time from surgery to death caused by disease. Survival data were censored on 15 September 2022. Survival curves were plotted using the Kaplan–Meier method and compared using the Mantel–Cox log rank test. Cox proportional hazards regression was used for survival analysis. Carbohydrate antigen 19-9 (CA 19-9) is the primary serum biomarker used in ICC management; however, its optimal prognostic cut-off value has yet to be identified.[5] We therefore used X-tile 3.6.1 software (Yale University School of Medicine, New Haven, CT, USA) to determine the easy-to-remember cut-off value of CA 19-9 based on training data (Fig. S2). Other laboratory parameters were dichotomised for Cox regression analysis according to the corresponding normal thresholds that are also compatible with previous publications.[17,20]

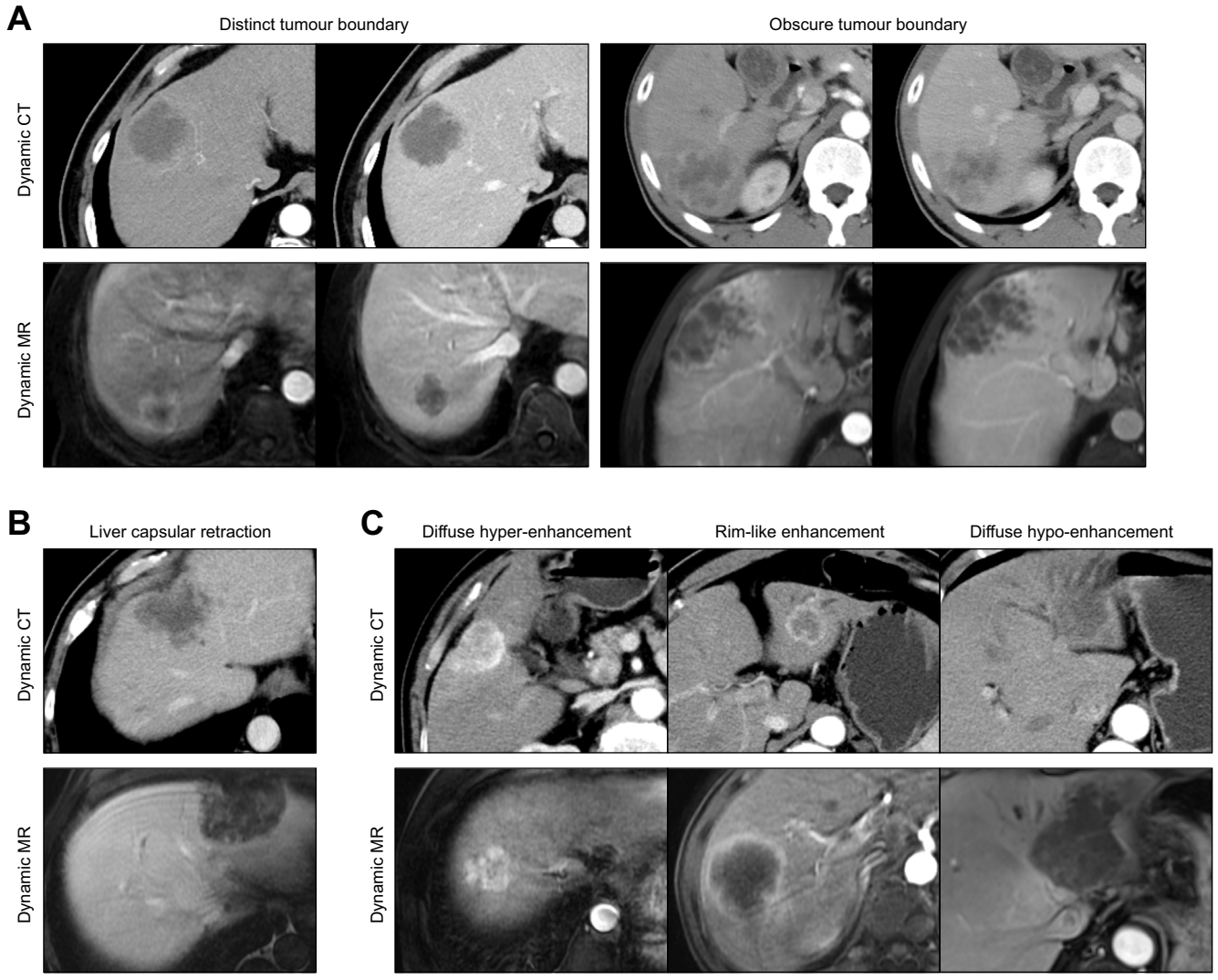

Fig. 2. Summary of CT and MR major traits in MICC-RACS systems. (A) Distinct tumour boundary was defined as a regular and smooth border at either the arterial or venous phase; obscure tumour boundary was defined as an irregular and ill-defined border at either the arterial or venous phase. (B) Liver capsular retraction was defined as focal invagination of the typical smooth contour of the liver capsule. (C) Diffuse hyperenhancement was defined as the hyperenhanced area that was >70% of the tumour volume at the arterial phase; peripheral rim enhancement was defined as the ring-like hyperenhanced area that measured 10–70% of the tumour volume with relatively hypoenhanced central areas at the arterial phase. CT, computed tomography; MICC-RACS, radiological and clinical scoring for mass-forming intrahepatic cholangiocarcinoma; MR, magnetic resonance.

Modelling strategies for radiological and clinical scoring (RACS) systems are as follows: (1) Significant factors related to both DFS and DSS in the univariable analysis were considered for the multivariable Cox model using backward stepwise elimination with the Akaike information criterion. The proportional hazards assumption in Cox regression was confirmed by examining the scaled Schoenfeld residual plots. (2) Regression coefficients of the multivariate Cox model were rounded to the nearest integer that can reflect the relative impact of model components and facilitate bedside calculation of the prognostic score. The integer value for each model covariable was then summed to calculate the MICC-RACS score. Two MICC-RACS systems were developed: one included parameters available before surgery so as to allow preoperative prognosis prediction; the other included the aforementioned parameters plus pathological variables after resection for more accurate predictions. Model performance was evaluated based on discrimination (measured by Harrell's C-statistic) and calibration (depicted by calibration plot). We evaluated the prognostic performance of novel scoring systems in an independent external cohort to avoid overoptimistic results caused by model fitting and assessment in the same dataset. Statistical analyses were performed using R software (R Foundation for Statistical Computing, Vienna, Austria; version 3.4.4, http://www.r-project.org). A p value <0.05 indicated statistical significance.

Results

Patient characteristics

Among 322 patients included in the model training/validation, 218 (67.7%) patients had a recurrence after resection, and 179 (55.6%) tumour-related deaths were recorded during a median

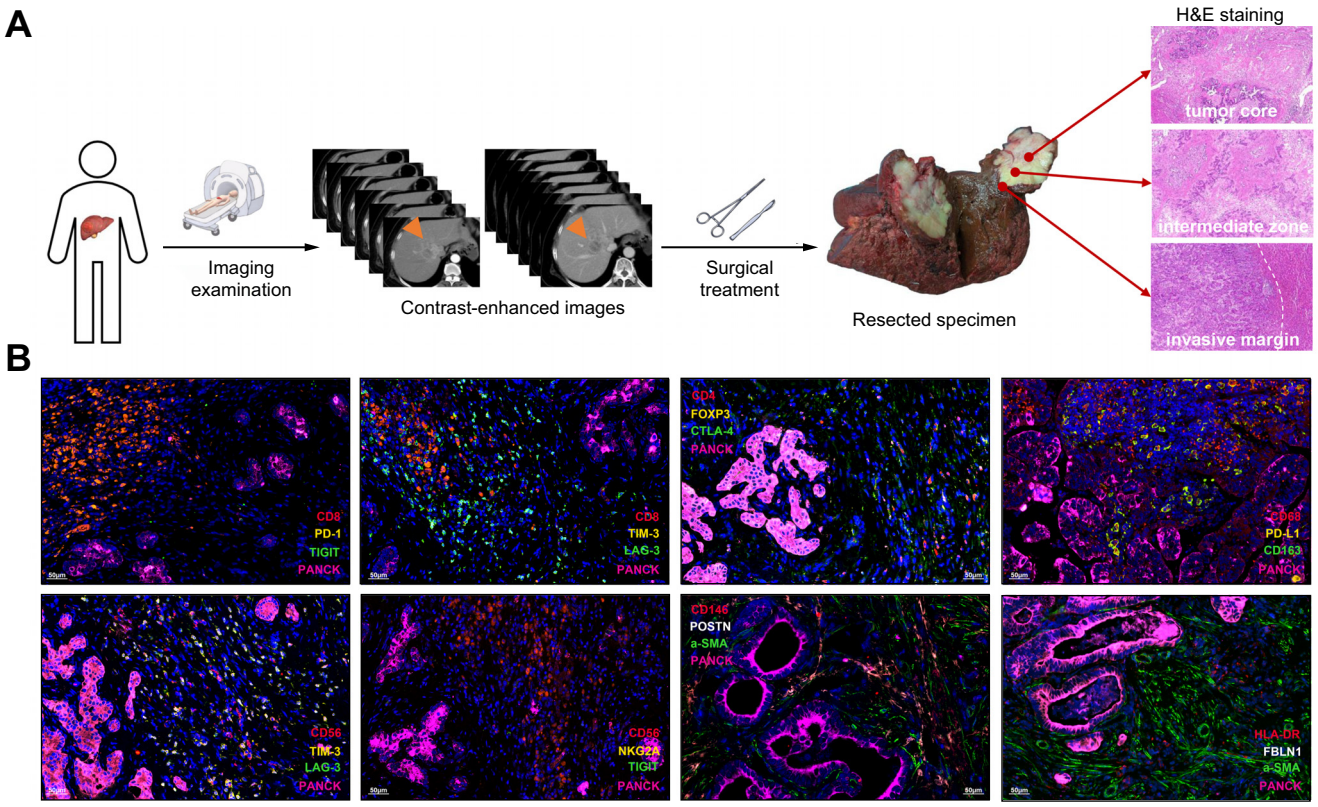

Fig. 3. Identification and characterisation of tumour-infiltrating immune cells and CAFs in MICC tissues. (A) Schematic representation of the experimental design. (B) Representative composite images of the multiplex immunofluorescence panels used in this study. CAF, cancer-associated fibroblast; MICC, mass-forming intrahepatic cholangiocarcinoma.

follow-up of 31.1 months (IQR, 13.3–56.1 months). Kaplan–Meier estimates of DSS rates were 51.1 and 43.9% at 3 and 5 years, respectively, and DFS rates were 37.7 and 34.1% at 3 and 5 years, respectively. Baseline clinicopathological characteristics and radiological findings of the training/validation cohort are shown in Table S1.

Training–validation–testing of the MICC-RACS systems

Among all clinical–radiological–pathological variables analysed, 18 significant predictors of both DFS and DSS, including three clinical factors (albumin [ALB], carcinoembryonic antigen, and CA 19-9), five conventional imaging traits (tumour number, maximum tumour diameter, liver cirrhosis, vascular invasion, and radiological nodal status), five characteristic imaging traits (gross type, tumour boundary status, liver capsular retraction, arterial enhancement pattern, and enhancing capsule), and five pathological characteristics (margin status, vascular invasion, pathological nodal status, perforating visceral peritoneum, and tumour necrosis), were identified by univariate analysis (Table 1). Table 2 shows the multivariate Cox models with backward elimination of categorised covariables used to develop the points-based scoring systems. Regression coefficients were then converted into scores where CA19-9 >300 IU/ml, ALB ≤40 g/L, multiple lesions, obscure tumour boundary, liver capsular retraction, nodal status on imaging or pathology, and tumour necrosis on pathology were each assigned a score of 1.0 (β-estimate, 0.400–0.913), whereas peripheral rim enhancement and diffuse hypoenhancement were assigned a score of 2.0 (β-estimate, 1.281–1.465) and 3.0 (β-estimate, 1.593–1.972), respectively. The preoperative and postoperative MICC-RACS systems are depicted in simplified layout in Fig. 4A. Correspondingly, two clinical scoring systems that integrated independent predictors available before or after surgery without the addition of any characteristic imaging trait were also developed (Table S2).

In the training cohort, the C-statistics of the preoperative MICC-RACS system for predicting DSS and DFS were 0.808 (95% CI 0.770–0.846) and 0.782 (95% CI 0.745–0.818), which were superior (p <0.05) to those of a preoperative clinical model and Fudan score.[17] The postoperative MICC-RACS system yielded the best discriminatory ability, with respective C-statistics of 0.821 (95% CI 0.785–0.857) and 0.789 (95% CI 0.754–0.824) for predicting DSS and DFS, which exceeded (p <0.05) those of a postoperative clinical model, the MEGNA score,[8] the Hyder *et al.*[7] model, the Wang *et al.*[6] model, and the TNM systems (seventh and eighth editions). The calibration plots demonstrated close agreement between the predicted and observed survival probabilities (Fig. S3A). In the validation cohort, the MICC-RACS systems had similar C-statistics and calibration accuracy (Table 3 and Fig. S3B). Interobserver agreement for the three characteristic imaging traits integrated into MICC-RACS systems were good to excellent on both CT and MR (k = 0.77 and 0.91 for arterial enhancement pattern, 0.86 and 0.87 for tumour boundary, and 0.76 and 0.86 for capsular retraction, respectively). The MICC-RACS systems also exhibited good

Table 1. Association of clinical–radiological–pathological characteristics with survival in the training cohort.

Characteristic	Disease-specific survival		Disease-free survival	
	Hazard ratio	*p* value	Hazard ratio	*p* value
Patient demographics				
Age (>60 *vs.* ≤60 years)	1.167 (0.792–1.720)	0.435	0.944 (0.668–1.334)	0.742
Sex (male *vs.* female)	1.239 (0.839–1.830)	0.280	1.079 (0.762–1.528)	0.668
HBV infection (present *vs.* absent)	0.611 (0.362–1.031)	0.065	0.601 (0.373–0.970)	0.037
Laboratory parameters				
ALT (>50 *vs.* ≤50 U/L)	1.388 (0.844–2.284)	0.197	1.058 (0.663–1.688)	0.814
AST (>40 *vs.* ≤40 U/L)	1.218 (0.754–1.967)	0.420	1.015 (0.647–1.594)	0.948
ALB (>40 *vs.* ≤40 g/L)	0.460 (0.322–0.657)	<0.001	0.606 (0.437–0.839)	0.003
TBIL (>19 *vs.* ≤19 μmol/L)	1.472 (0.937–2.313)	0.093	1.202 (0.791–1.828)	0.388
CEA (>5 *vs.* ≤5 ng/ml)	2.212 (1.500–3.262)	<0.001	1.703 (1.193–2.431)	0.003
CA19-9 (>300 *vs.* ≤300 IU/ml)	3.771 (2.511–5.662)	<0.001	3.772 (2.596–5.481)	<0.001
Conventional imaging traits				
Tumour location (perihilar *vs.* peripheral)	1.609 (1.025–2.525)	0.039	1.251 (0.818–1.913)	0.302
Tumour number (multiple *vs.* solitary)	2.386 (1.578–3.608)	<0.001	2.674 (1.840–3.888)	<0.001
Maximum tumour diameter (>5 *vs.* ≤5 cm)	1.909 (1.282–2.843)	0.001	2.240 (1.566–3.203)	<0.001
Liver cirrhosis (present *vs.* absent)	0.512 (0.266–0.984)	0.044	0.521 (0.293–0.925)	0.026
Peritumoural biliary dilatation (present *vs.* absent)	1.623 (1.103–2.387)	0.014	1.390 (0.983–1.965)	0.063
Vascular invasion (present *vs.* absent)	2.048 (1.379–3.042)	<0.001	1.876 (1.311–2.685)	<0.001
Lymph node metastasis (present *vs.* absent)	2.751 (1.854–4.081)	<0.001	2.856 (2.005–4.067)	<0.001
Characteristic imaging traits				
Gross type (ductal type *vs.* parenchymal type)	2.481 (1.563–3.939)	<0.001	1.706 (1.106–2.633)	0.016
Tumour boundary (obscure *vs.* distinct)	3.420 (2.303–5.079)	<0.001	3.284 (2.302–4.683)	<0.001
Liver capsule retraction (present *vs.* absent)	2.228 (1.509–3.292)	<0.001	2.233 (1.561–3.195)	<0.001
Arterial enhancement pattern				
Rim enhancement *vs.* hyperenhancement	6.139 (3.028–12.44)	<0.001	6.466 (3.645–11.47)	<0.001
hypoenhancement *vs.* hyperenhancement	13.65 (6.735–27.67)	<0.001	9.884 (5.563–17.56)	<0.001
Progressive enhancement (present *vs.* absent)	0.773 (0.502–1.189)	0.242	1.003 (0.690–1.457)	0.988
Enhancing capsule (present *vs.* absent)	0.445 (0.282–0.704)	*vs.*<0.001	0.450 (0.301–0.672)	<0.001
Peripheral washout (present *vs.* absent)	1.258 (0.755–2.095)	0.379	1.456 (0.927–2.288)	0.103
Histologic characteristics				
Edmondson grade (III–IV *vs.* I–II)	1.022 (0.620–1.685)	0.931	1.120 (0.718–1.746)	0.617
Surgical margin (R1 *vs.* R0)	2.231 (1.285–3.873)	0.004	4.574 (2.748–7.612)	<0.001
Perineural invasion (present *vs.* absent)	1.449 (0.939–2.239)	0.094	1.279 (0.861–1.900)	0.223
Satellite nodule (present *vs.* absent)	1.631 (0.943–2.822)	0.080	2.390 (1.569–3.640)	<0.001
Vascular invasion				
microvascular *vs.* none	1.307 (0.665–2.569)	0.438	1.398 (0.788–2.481)	0.252
macrovascular *vs.* none	2.127 (1.405–3.219)	<0.001	1.766 (1.208–2.582)	0.003
Lymph node metastasis (present *vs.* absent)	4.767 (3.161–7.189)	<0.001	4.231 (2.887–6.202)	<0.001
Perforating visceral peritoneum (present *vs.* absent)	2.234 (1.513–3.298)	<0.001	2.200 (1.542–3.138)	<0.001
Local extrahepatic invasion (present *vs.* absent)	0.821 (0.202–3.333)	0.783	1.341 (0.495–3.634)	0.564
Liver cirrhosis (present *vs.* absent)	0.607 (0.345–1.066)	0.083	0.626 (0.380–1.031)	0.066
Intratumoural necrosis (present *vs.* absent)	2.230 (1.422–3.498)	<0.001	2.127 (1.402–3.227)	<0.001
Adjuvant chemotherapy/radiotherapy (yes *vs.* no)	0.479 (0.285–0.805)	0.006	0.843 (0.560–1.268)	0.412

Numbers in parentheses are the 95% CIs. Levels of significance: p <0.05 (Cox proportional hazards model).
ALB, albumin; ALT, alanine aminotransferase; AST, aspartate aminotransferase; CA19-9, carbohydrate antigen 19-9; CEA, carcinoembryonic antigen; TBIL, total bilirubin.

prognostic discrimination across imaging modalities (C-statistic range of 0.778–0.814 and 0.763–0.824 for CT and MR imaging, respectively).

Calculated MICC-RACS scores ranged from 0 to 10, and each patient was assigned to one of three risk groups according to the cut points as follows: low risk (0–2), medium risk (3–5), and high risk (≥6). Patients with a preoperative MICC-RACS score of 0–2, 3–5, and ≥6 had incrementally worse 5-year DSS and DFS (96.1 and 80.7% *vs.* 31.6 and 13.3% *vs.* 5.1 and 0.0%, respectively; p <0.001) in the training cohort (Table S3). Similarly, the postoperative MICC-RACS system categorised patients from the training cohort into three separate prognostic groups according to the prespecified cut points (Table S4). Similar results were found in the independent validation cohort (Tables S3 and S4). Survival curves for the entire cohort stratified by MICC-RACS systems are shown in Fig. 4B and C.

TIME characteristics underlying radiological traits

Spatial analysis of MICC samples revealed that tumour-infiltrating immune cells were enriched within tumour stroma and at the invasive margin, but were scarce within the tumour epithelium and at the tumour core. Collectively, $CD8^+$ T and NK cells exhibited high expression of inhibitory markers (PD-1, TIM-3, LAG-3, TIGIT, and NKG2A), suggesting that cytotoxic effector cells became exhausted, accompanied by high infiltration of immunosuppressive tumour-infiltrating Tregs ($CD4^+FOXP3^+$) and anti-inflammatory M2-like macrophages ($CD68^+CD163^+$). In addition, high abundance of $CD146^+$ vascular CAFs was observed within the stromal compartment of tumours, whereas $POSTN^+$ matrix CAFs were mainly localised at the tumour core and intermediate zone (Fig. S4).

We next sought to explore the associations between TIME heterogeneity and radiological traits. Significant differences in

Table 2. Multivariable Cox regression analysis of factors associated with patient survival using stepwise backward selection method.

Variable	Preoperative model			Postoperative model		
	β	Hazard ratio	*p* value	β	Hazard ratio	*p* value
Disease-specific survival						
CA19-9 >300 IU/ml	0.597	1.816 (1.157–2.851)	0.009	0.588	1.801 (1.135–2.858)	0.012
ALB ≤40 g/L	0.913	2.490 (1.647–3.765)	<0.001	0.735	2.085 (1.344–3.234)	0.001
Multiple lesions	0.569	1.766 (1.158–2.694)	0.008	0.571	1.770 (1.154–2.715)	0.009
LNM on imaging	0.439	1.551 (1.001–2.402)	0.049	NA	NA	NA
Obscure tumour boundary	0.581	1.787 (1.183–2.698)	0.006	0.580	1.786 (1.182–2.700)	0.006
Liver capsule retraction	0.600	1.822 (1.190–2.789)	0.006	0.512	1.668 (1.089–2.557)	0.019
Arterial enhancement pattern						
Rim enhancement *vs.* hyperenhancement	1.379	3.935 (1.859–8.329)	<0.001	1.281	3.601 (1.688–7.684)	<0.001
Hypoenhancement *vs.* hyperenhancement	1.940	6.956 (3.231–14.98)	<0.001	1.972	7.184 (3.335–15.48)	<0.001
LNM on pathology	NA	NA	NA	0.615	1.850 (1.182–2.898)	0.007
Necrosis on pathology	NA	NA	NA	0.586	1.797 (1.094–2.954)	0.021
AIC		872.22			865.91	
Disease-free survival						
CA19-9 >300 IU/ml	0.645	1.906 (1.251–2.906)	0.003	0.658	1.931 (1.256–2.970)	0.003
ALB ≤40 g/L	0.512	1.668 (1.151–2.418)	0.007	0.403	1.497 (1.013–2.212)	0.043
Multiple lesions	0.571	1.770 (1.214–2.580)	0.003	0.470	1.600 (1.074–2.383)	0.021
LNM on imaging	0.420	1.522 (1.012–2.287)	0.044	NA	NA	NA
Obscure tumour boundary	0.525	1.690 (1.146–2.491)	0.008	0.516	1.675 (1.136–2.470)	0.009
Liver capsule retraction	0.532	1.703 (1.158–2.504)	0.007	0.400	1.492 (1.022–2.177)	0.038
Arterial enhancement pattern						
Rim enhancement *vs.* hyperenhancement	1.452	4.272 (2.327–7.841)	<0.001	1.465	4.326 (2.356–7.945)	<0.001
Hypoenhancement *vs.* hyperenhancement	1.593	4.918 (2.614–9.253)	<0.001	1.677	5.347 (2.856–10.01)	<0.001
LNM on pathology	NA	NA	NA	0.500	1.649 (1.070–2.543)	0.024
Necrosis on pathology	NA	NA	NA	0.490	1.633 (1.022–2.610)	0.040
AIC		1,104.36			1,101.71	

Numbers in parentheses are the 95% CIs. Levels of significance: p <0.05 (Cox proportional hazards model).
AIC, Akaike information criteria; ALB, albumin; CA19-9, carbohydrate antigen 19-9; LNM, lymph node metastasis; NA, not applicable.

the infiltration level and spatial distribution of immune cells were found between arterial enhancement patterns (Fig. 5). Specifically, diffuse hyperenhancement tumours were broadly populated with immune cells expressing a certain number of exhaustion or immunosuppression markers from the tumour core to the invasive margin. However, rim-like enhancement tumours were characterised by high infiltration of immune cells at the invasive margin. Diffuse hypoenhancement tumours were poorly infiltrated by immune cells but expressed higher $CD146^{+}$ vascular CAFs than the other two enhancement patterns. As expected, the density of immune cell infiltration was relatively higher in patients with distinct tumour boundary than in those with obscure tumour boundary (Fig. S5). Interestingly, significantly higher infiltration of macrophages, activated predominantly as M2 phenotype, at the invasive margin was noted in tumours with capsular retraction than in those without (Fig. S6).

Discussion

Patients with MICC are at substantial risk for recurrence and death, even after curative-intent resection. Reliable prognostic tools are therefore needed to select patients who have poor survival outcomes before and after surgery and who might benefit from additional neoadjuvant/adjuvant therapy. In this study, we developed the readily applicable MICC-RACS systems – based on two serum parameters (CA19-9 and ALB), two conventional imaging traits (tumour number and radiological nodal status), three characteristic imaging traits (tumour boundary status, liver capsular retraction, and arterial enhancement pattern), and two pathological characteristics (pathological nodal status and tumuor necrosis) – and validated them in an independent dataset across different imaging modalities. The MICC-RACS systems exhibited excellent discriminatory power with respective C-statistics of 0.802–0.821 and 0.756–0.789 for predicting DSS and DFS, and had substantially improved performance over rival prognostic models and present staging systems across study cohorts. Our new scoring systems can further stratify patients into three subgroups with discrete risk profiles in both preoperative and postoperative settings. Moreover, we have elucidated for the first time the association between prognostic imaging traits and highly heterogeneous TIME of MICC that allows robust inference from both directions and clinical translation with therapeutic implications for this difficult-to-treat disease.

Typically, dynamic CT or MR scanning of MICC yields early peripheral rim enhancement coupled with progressive centripetal enhancement, which can be explained by the cancer cells with abundant blood supply at the tumour periphery and the desmoplastic stroma with sparse cancer cells at the tumour center.[2,21] However, atypical enhancement patterns that may reflect the areal proportion and spatial distribution of cancer cells, fibrous stroma, necrosis, and mucin are frequently observed in MICCs.[21,22] Small-scale studies have suggested that hypovascular MICCs show more aggressive biology and worse post-resection prognosis than hypervascular MICCs.[13,23] We highlighted three patterns of arterial enhancement and a remarkable trend toward improved prognosis with increasing

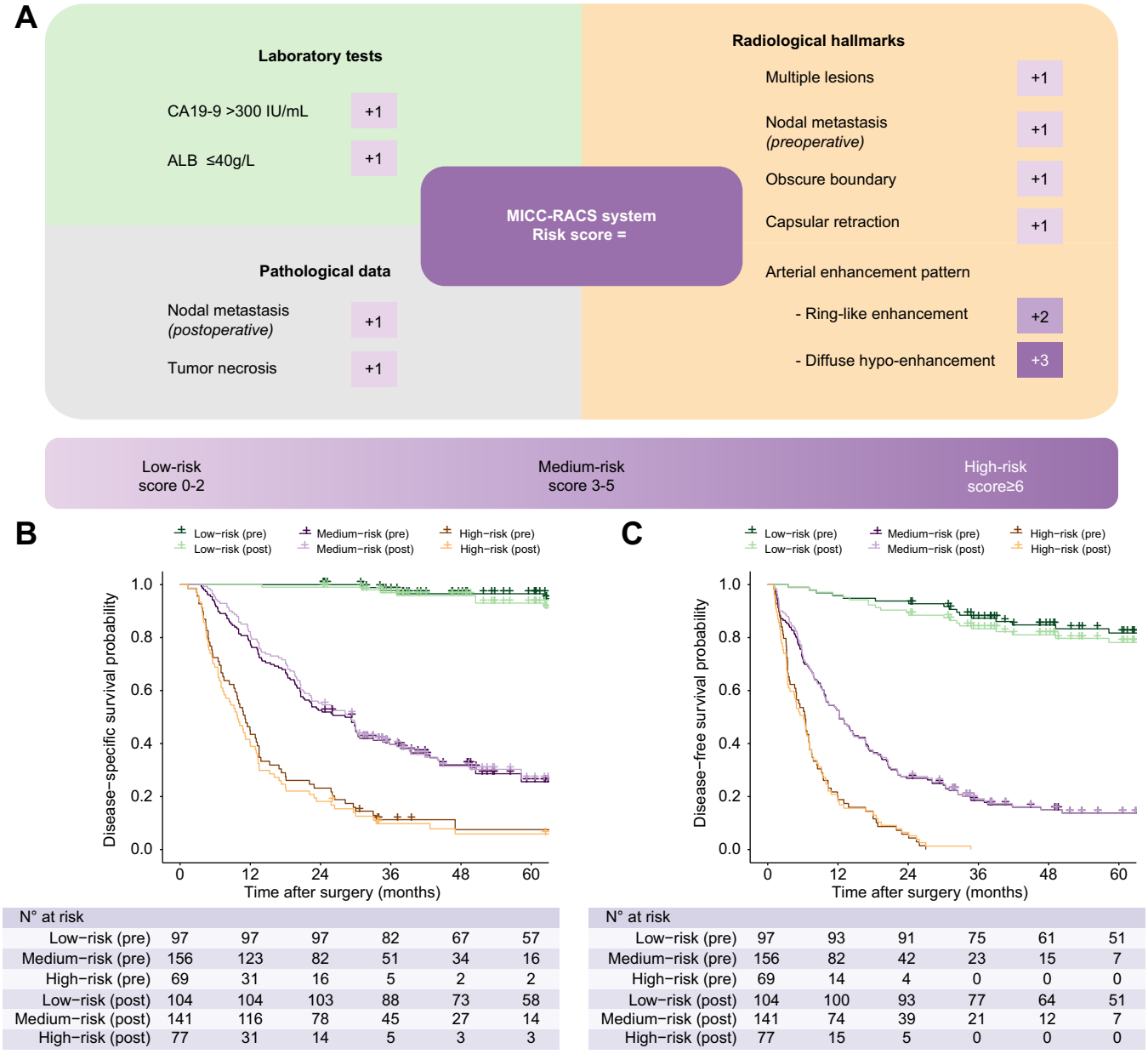

N° at risk						
Low−risk (pre)	97	97	97	82	67	57
Medium−risk (pre)	156	123	82	51	34	16
High−risk (pre)	69	31	16	5	2	2
Low−risk (post)	104	104	103	88	73	58
Medium−risk (post)	141	116	78	45	27	14
High−risk (post)	77	31	14	5	3	3

N° at risk						
Low−risk (pre)	97	93	91	75	61	51
Medium−risk (pre)	156	82	42	23	15	7
High−risk (pre)	69	14	4	0	0	0
Low−risk (post)	104	100	93	77	64	51
Medium−risk (post)	141	74	39	21	12	7
High−risk (post)	77	15	5	0	0	0

Fig. 4. MICC-RACS calculator. (A) Risk score is the sum of points assigned to each predictor. Note that nodal status is determined either by imaging in the preoperative system or by pathology in the postoperative system. (B) Kaplan–Meier curves of disease-specific survival stratified according to MICC-RACS calculator in the entire cohort. (C) Kaplan–Meier curves of disease-free survival stratified according to MICC-RACS calculator in the entire cohort. ALB, albumin; CA-19, carbohydrate antigen 19-9; MICC-RACS, radiological and clinical scoring for mass-forming intrahepatic cholangiocarcinoma.

enhancement (from diffuse hypoenhancement to rim-like enhancement to diffuse hyperenhancement) on both CT and MR. These results are in good agreement with previous studies based on either CT or MR.[14,24] Next, we focused specifically on tumour-infiltrating immune cells and immune checkpoint markers as an initial step in decoding the TIME of MICCs by non-invasive imaging considering the low rate of ICC responses to immune checkpoint inhibitors (ICIs) in early clinical trials. We found that MICCs with diffuse hyperenhancement trended toward immune 'hot' profiles, but, as expected, overexpressed immune checkpoint molecules may be associated with higher response rates to ICIs in an adjuvant/neoadjuvant setting. Notably, a highly infiltrated microenvironment at the invasive margin in MICCs with rim-like enhancement suggests that the area of arterial contrast enhancement is consistent with the abundance of immune infiltration. Given that diffuse hypovascular MICCs exhibited 'cold' immune profiles, strategies to therapeutically target the TIME include a prior combination of

Table 3. Performance of MICC-RACS systems compared with rival models and staging systems for predicting post-resection survival.

Model	Disease-specific survival		Disease-free survival	
	C-statistic	*p* value	C-statistic	*p* value
Training cohort (n = 193)				
Preoperative MICC-RACS system	0.808 (0.770–0.846)	Reference	0.782 (0.745–0.818)	Reference
Postoperative MICC-RACS system	0.821 (0.785–0.857)	Reference	0.789 (0.754–0.824)	Reference
Preoperative clinical model	0.747 (0.701–0.792)	<0.001*	0.732 (0.694–0.770)	0.007*
Postoperative clinical model	0.772 (0.729–0.815)	0.005†	0.750 (0.714–0.786)	0.037†
Fudan score	0.705 (0.660–0.750)	<0.001*	0.699 (0.660–0.737)	<0.001*
MEGNA score	0.646 (0.597–0.695)	<0.001†	0.610 (0.566–0.653)	<0.001†
Hyder model	0.698 (0.646–0.750)	<0.001†	0.672 (0.625–0.718)	<0.001†
Wang model	0.733 (0.686–0.779)	<0.001†	0.720 (0.678–0.763)	<0.001†
LCSGJ system	0.710 (0.664–0.756)	<0.001†	0.679 (0.637–0.721)	<0.001†
TNM system, seventh edition	0.698 (0.648–0.748)	<0.001†	0.685 (0.642–0.729)	<0.001†
TNM system, eighth edition	0.705 (0.655–0.754)	<0.001†	0.689 (0.646–0.732)	<0.001†
Validation cohort (n = 129)				
Preoperative MICC-RACS system	0.802 (0.755–0.848)	Reference	0.759 (0.710–0.808)	Reference
Postoperative MICC-RACS system	0.813 (0.766–0.860)	Reference	0.756 (0.706–0.806)	Reference
Preoperative clinical model	0.682 (0.622–0.742)	<0.001*	0.665 (0.608–0.723)	<0.001*
Postoperative clinical model	0.714 (0.658–0.769)	<0.001†	0.670 (0.617–0.723)	<0.001†
Fudan score	0.717 (0.660–0.774)	0.004*	0.677 (0.619–0.734)	0.010*
MEGNA score	0.662 (0.606–0.718)	<0.001†	0.624 (0.569–0.679)	<0.001†
Hyder model	0.712 (0.656–0.769)	0.001†	0.641 (0.589–0.694)	<0.001†
Wang model	0.717 (0.663–0.771)	<0.001†	0.661 (0.608–0.715)	<0.001†
LCSGJ system	0.713 (0.664–0.763)	<0.001†	0.647 (0.597–0.696)	<0.001†
TNM system, seventh edition	0.703 (0.647–0.759)	<0.001†	0.635 (0.584–0.686)	<0.001†
TNM system, eighth edition	0.705 (0.649–0.760)	<0.001†	0.637 (0.586–0.689)	<0.001†

Numbers in parentheses are the 95% CIs. Levels of significance: p <0.05 (by 'compareC' package in R software).
LCSGJ, Liver Cancer Study Group of Japan; MICC-RACS, radiological and clinical scoring for mass-forming intrahepatic cholangiocarcinoma; TNM, tumour–node–metastasis.
* p value *vs.* the preoperative system.
† p value *vs.* the postoperative system.

therapies using various cytotoxic and modulating agents to potentiate immune-cell infiltration and then ICIs to boost anti-tumour immune responses.[25,26] Intriguingly, we here identified that diffuse hypovascular tumours expressed high levels of $CD146^+$ vascular CAFs, which are known to interact with malignant cells to promote ICC progression via IL-6/IL-6 receptor axis, a potential druggable target.[19,27]

We also found that obscure tumour boundary is suggestive of poor prognosis in MICC patients, consistent with previous reports.[17,28] Relatively low numbers of $CD8^+$ T-cell infiltration from the tumour core to the invasive margin were noted in MICCs with obscure boundary as compared with those with distinct boundary. Interestingly, however, MICCs with distinct boundary were accompanied by enhanced infiltration of Tregs, a highly immunosuppressive subset of $CD4^+$ T cells, at both the tumour core and the invasive margin, suggesting that manipulation of Tregs could facilitate immune precision medicine for the individual patient because ICIs targeting PD-1 might enhance the immunosuppressive function of Tregs, whereas CTLA-4 inhibitors might deplete these cells.[29,30] In addition, retraction of the liver capsular has been traditionally thought to be caused by chronic bile duct obstruction and adjacent liver parenchyma atrophy induced by MICCs.[31] Here, we identified an association of liver capsular retraction with significantly increased infiltration of M2-like macrophages, which are generally considered to be immunosuppressive, at the invasive margin; therefore, concerning the MICC with capsular retraction on cross-sectional imaging, macrophage-focused therapeutic strategies hold the potential to complement and synergise with both chemotherapy and ICI therapy.[32]

There are limitations of the present study. First, care should be taken before generalising our findings to other populations because our data are retrospective and from China. Second, a relatively small sample size in TIME evaluation as compared with model training/validation may limit the statistical significance and cause biased results in some comparisons. Third, there may be slight variations in the assessment of radiological traits using different imaging modalities (CT or MR); however, the discrepancies are unlikely to be clinically significant.[33] It is the fact that the choice of modality (CT or MR) and MR contrast agent (extracellular or hepatobiliary) depends on several factors, such as patient, institution, and region; however, our MICC-RACS systems are not confined to any specific imaging method. Fourth, the validation cohort used in the study is a random subset of the recruitment, and there is a lack of a large-scale external dataset as a validation cohort, although we enrolled patients from multiple institutions over a long period of time for a relatively large sample size. Finally, we failed to discover an immunotherapy cohort to validate our results about imaging trait-guided immunotherapy options in MICCs.

In conclusion, our MICC-RACS systems are powerful and easy-to-use tools to predict the prognosis of MICC patients either before or after surgery. The high efficiency of MICC-RACS systems relies on the inclusion of three imaging traits (arterial enhancement pattern, tumour boundary, and capsular retraction) that are associated with spatially distinct TIMEs, thereby renovating the treatment paradigm and improving clinical outcomes of MICCs. Further studies are needed to verify our findings.

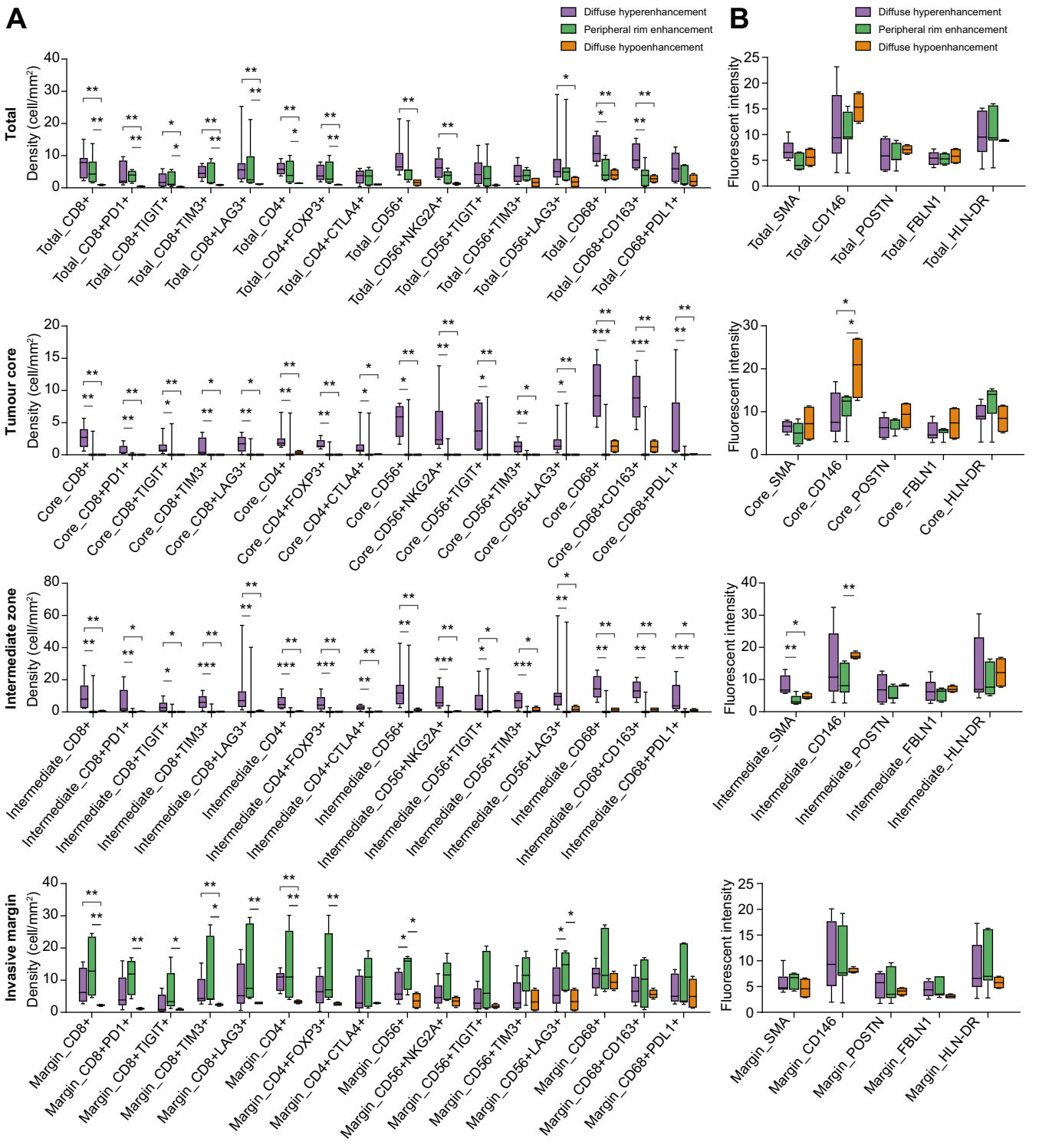

Fig. 5. Distinct TIME characteristics underlying arterial enhancement patterns. (A) Densities of indicated immune cells across the regions of interest. Levels of significance: ***p <0.001; **p <0.01; *p <0.05 (Mann–Whitney U test). (B) Intensities of indicated CAF markers across the regions of interest. Levels of significance: ***p <0.001; **p <0.01; *p <0.05 (Mann–Whitney U test). CAF, cancer-associated fibroblast; TIME, tumour immune microenvironment.

Abbreviations

AIC, Akaike information criteria; ALB, albumin; ALT, alanine aminotransferase; AST, aspartate aminotransferase; CA19-9, carbohydrate antigen 19-9; CAF, cancer-associated fibroblast; CEA, carcinoembryonic antigen; CTLA-4, cytotoxic T lymphocyte antigen-4; DFS, disease-free survival; DSS, disease-specific survival; ICI, immune checkpoint inhibitor; LAG-3, lymphocyte-activation gene 3; LCSGJ, Liver Cancer Study Group of Japan; LNM, lymph node metastasis; MICC-RACS, radiological and clinical scoring for mass-forming intrahepatic cholangiocarcinoma; MICC, mass-forming intrahepatic cholangiocarcinoma; NK, natural killer; NKG2A, NK group 2 member A; PD-1, programmed death 1; PD-L1, programmed death ligand 1; RACS, radiological and clinical scoring; TBIL, total bilirubin; TIGIT, T-cell Ig and immunoreceptor tyrosine-based inhibitory motif domain; TIM-3, T-cell Ig and mucin domain-3 protein; TIME, tumour immune microenvironment; TNM, tumour–node–metastasis; Treg, regulatory T cell.

Financial support

This work was supported by the Key Program of the National Natural Science Foundation of China (31930020), the National Natural Science Foundation of China (82102150), and the Natural Science Foundation of Jiangsu Province (BK20210968).

Conflicts of interest

The authors have no relevant financial or non-financial interests to disclose.

Please refer to the accompanying ICMJE disclosure forms for further details.

Authors' contributions

Contributed to drafting of this manuscript: GWJ. Contributed to radiological evaluation: GWJ, QX, CYJ, ML. Was responsible for analysis and interpretation of data: ZGX. Collected data: ZGX, BZ, YY. Contributed to study concept and design, and critical revision for the draft manuscript: KW, XCL, XHW. Approved the final version of this manuscript: all authors.

Data availability statement

Data generated or analysed during the study are available from the corresponding author by request.

Acknowledgements

The authors thank Dr Jin-Song Wang and Dr Wen-Bin Huang for the assistance in multiplex analysis.

Supplementary data

Supplementary data to this article can be found online at https://doi.org/10.1016/j.jhepr.2023.100839.

References

Author names in bold designate shared co-first authorship

[1] Banales JM, Marin JJG, Lamarca A, Rodrigues PM, Khan SA, Roberts LR, et al. Cholangiocarcinoma 2020: the next horizon in mechanisms and management. Nat Rev Gastroenterol Hepatol 2020;17:557–588.

[2] Brindley PJ, Bachini M, Ilyas SI, Khan SA, Loukas A, Sirica AE, et al. Cholangiocarcinoma Nat Rev Dis Primers 2021;7:65.

[3] Bridgewater J, Galle PR, Khan SA, Llovet JM, Park JW, Patel T, et al. Guidelines for the diagnosis and management of intrahepatic cholangiocarcinoma. J Hepatol 2014;60:1268–1289.

[4] Valle JW, Kelley RK, Nervi B, Oh DY, Zhu AX. Biliary tract cancer. Lancet 2021;397:428–444.

[5] Mazzaferro V, Gorgen A, Roayaie S, Droz Dit Busset M, Sapisochin G. Liver resection and transplantation for intrahepatic cholangiocarcinoma. J Hepatol 2020;72:364–377.

[6] **Wang Y**, **Li J**, **Xia Y**, Gong R, Wang K, Yan Z, et al. Prognostic nomogram for intrahepatic cholangiocarcinoma after partial hepatectomy. J Clin Oncol 2013;31:1188–1195.

[7] Hyder O, Marques H, Pulitano C, Marsh JW, Alexandrescu S, Bauer TW, et al. A nomogram to predict long-term survival after resection for intrahepatic cholangiocarcinoma: an Eastern and Western experience. JAMA Surg 2014;149:432–438.

[8] Raoof M, Dumitra S, Ituarte PHG, Melstrom L, Warner SG, Fong Y, et al. Development and validation of a prognostic score for intrahepatic cholangiocarcinoma. JAMA Surg 2017;152:e170117.

[9] **Büttner S**, **Galjart B**, Beumer BR, van Vugt JLA, van Eijck CHJ, Polak WG, et al. Quality and performance of validated prognostic models for survival after resection of intrahepatic cholangiocarcinoma: a systematic review and meta-analysis. HPB (Oxford) 2021;23:25–36.

[10] **Zhang S**, **Huo L**, Feng Y, Zhang J, Wu Y, Liu Y, et al. Preoperative differentiation of hepatocellular carcinoma with peripheral rim-like enhancement from intrahepatic mass-forming cholangiocarcinoma on contrast-enhanced MRI. Front Oncol 2022;12:986713.

[11] Xing LH, Zhuo LY, Wang JN, Zhang Y, Zhu FY, Wang C, et al. Values of MRI imaging presentations in the hepatobiliary phase, DWI and T2WI sequences in predicting pathological grades of intrahepatic mass-forming cholangiocarcinoma. Front Oncol 2022;12:867702.

[12] Xiao Y, Zhou C, Ni X, Huang P, Wu F, Yang C, et al. Preoperative subcategorization based on magnetic resonance imaging in intrahepatic cholangiocarcinoma. Cancer Imaging 2023;23:15.

[13] Fujita N, Asayama Y, Nishie A, Ishigami K, Ushijima Y, Takayama Y, et al. Mass-forming intrahepatic cholangiocarcinoma: enhancement patterns in the arterial phase of dynamic hepatic CT - correlation with clinicopathological findings. Eur Radiol 2017;27:498–506.

[14] Min JH, Kim YK, Choi SY, Kang TW, Lee SJ, Kim JM, et al. Intrahepatic mass-forming cholangiocarcinoma: arterial enhancement patterns at MRI and prognosis. Radiology 2019;290:691–699.

[15] Rhee H, Choi SH, Park JH, Cho ES, Yeom SK, Park S, et al. Preoperative magnetic resonance imaging-based prognostic model for mass-forming intrahepatic cholangiocarcinoma. Liver Int 2022;42:930–941.

[16] Rhee H, Kim MJ, Park YN, An C. A proposal of imaging classification of intrahepatic mass-forming cholangiocarcinoma into ductal and parenchymal types: clinicopathologic significance. Eur Radiol 2019;29:3111–3121.

[17] Jiang W, Zeng ZC, Tang ZY, Fan J, Sun HC, Zhou J, et al. A prognostic scoring system based on clinical features of intrahepatic cholangiocarcinoma: the Fudan score. Ann Oncol 2011;22:1644–1652.

[18] Ji GW, Zhang YD, Zhang H, Zhu FP, Wang K, Xia YX, et al. Biliary tract cancer at CT: a radiomics-based model to predict lymph node metastasis and survival outcomes. Radiology 2019;290:90–98.

[19] **Zhang M**, **Yang H**, **Wan L**, **Wang Z**, **Wang H**, Ge C, et al. Single-cell transcriptomic architecture and intercellular crosstalk of human intrahepatic cholangiocarcinoma. J Hepatol 2020;73:1118–1130.

[20] **Xu X**, **Zhang HL**, Liu QP, Sun SW, Zhang J, Zhu FP, et al. Radiomic analysis of contrast-enhanced CT predicts microvascular invasion and outcome in hepatocellular carcinoma. J Hepatol 2019;70:1133–1144.

[21] Joo I, Lee JM, Yoon JH. Imaging diagnosis of intrahepatic and perihilar cholangiocarcinoma: recent advances and challenges. Radiology 2018;288:7–13.

[22] Kubo S, Shinkawa H, Asaoka Y, Ioka T, Igaki H, Izumi N, et al. Liver Cancer Study Group of Japan clinical practice guidelines for intrahepatic cholangiocarcinoma. Liver Cancer 2022;11:290–314.

[23] Türkoğlu MA, Yamamoto Y, Sugiura T, Okamura Y, Ito T, Ashida R, et al. The favorable prognosis after operative resection of hypervascular intrahepatic cholangiocarcinoma: a clinicopathologic and immunohistochemical study. Surgery 2016;160:683–690.

[24] Park HM, Jang HY, Lee DE, Kang MJ, Han SS, Kim SW, et al. Prognostic impact of tumor vascularity on CT in resectable intrahepatic cholangiocarcinoma. HPB (Oxford) 2022;24:359–369.

[25] Job S, Rapoud D, Dos Santos A, Gonzalez P, Desterke C, Pascal G, et al. Identification of four immune subtypes characterized by distinct composition and functions of tumor microenvironment in intrahepatic cholangiocarcinoma. Hepatology 2020;72:965–981.

[26] **Bejarano L**, **Jordão MJC**, Joyce JA. Therapeutic targeting of the tumor microenvironment. Cancer Discov 2021;11:933–959.

[27] Fabris L, Andersen JB, Fouassier L. Intrahepatic cholangiocarcinoma: a single-cell resolution unraveling the complexity of the tumor microenvironment. J Hepatol 2020;73:1007–1009.
[28] Park S, Lee Y, Kim H, Yu MH, Lee ES, Yoon JH, et al. Subtype Classification of intrahepatic cholangiocarcinoma using liver MR imaging features and its prognostic value. Liver Cancer 2022;11:233–246.
[29] Togashi Y, Shitara K, Nishikawa H. Regulatory T cells in cancer immunosuppression – implications for anticancer therapy. Nat Rev Clin Oncol 2019;16:356–371.
[30] **Alvisi G**, **Termanini A**, Soldani C, Portale F, Carriero R, Pilipow K, et al. Multimodal single-cell profiling of intrahepatic cholangiocarcinoma defines hyperactivated Tregs as a potential therapeutic target. J Hepatol 2022;77:1359–1372.
[31] Panick CEP, Ward RD, Coppa C, Liu PS. Hepatic capsular retraction: an updated MR imaging review. Eur J Radiol 2019;113:15–23.
[32] Mantovani A, Marchesi F, Malesci A, Laghi L, Allavena P. Tumour-associated macrophages as treatment targets in oncology. Nat Rev Clin Oncol 2017;14:399–416.
[33] Chernyak V, Fowler KJ, Kamaya A, Kielar AZ, Elsayes KM, Bashir MR, et al. Liver Imaging Reporting and Data System (LI-RADS) version 2018: imaging of hepatocellular carcinoma in at-risk patients. Radiology 2018;289:816–830.